agriculture

MDPI

Article

Early-Winter Thermal Responses of East–West and North–South Tomato Ridge Layouts in a Chinese Solar Greenhouse

Zhihe Sun [1], Wenlu Shi [1], Mengmeng Yang [2,*], Qiyuan Wang [1], Xiaolong Dou [1], Yang Chen [3], Zhanyang Xu [1], Mingze Yao [1], Feng Zhang [1] and Wenhe Liu [1,4,*]

[1] College of Water Conservancy, Shenyang Agricultural University, Shenyang 110866, China; 2024240183@stu.syau.edu.cn (Z.S.); 2024200013@stu.syau.edu.cn (W.S.); 2025240186@stu.syau.edu.cn (Q.W.); 2025240181@stu.syau.edu.cn (X.D.); xuzhanyang@syau.edu.cn (Z.X.); yaomingze@syau.edu.cn (M.Y.); 2019500060@syau.edu.cn (F.Z.)
[2] College of Engineering, Shenyang Agricultural University, Shenyang 110866, China
[3] Capital Construction Office, Shenyang Agricultural University, Shenyang 110866, China; 2011500024@syau.edu.cn
[4] College of Ocean and Civil Engineering, Dalian Ocean University, Dalian 116023, China
* Correspondence: 2023500014@syau.edu.cn (M.Y.); liuwenhe@dlou.edu.cn (W.L.)

Abstract

This exploratory study compared early-winter thermal conditions in east–west (E-W) and north–south (N-S) tomato ridge blocks within one Chinese solar greenhouse from 22 November to 3 December 2025. A thin-film partition separated the blocks. We measured canopy-air, soil-surface, plastic-film, north-wall, and rear-slope temperatures and used transient computational fluid dynamics (CFD) to interpret spatial patterns. Mean canopy-air temperatures were 15.34 °C (E-W) and 15.22 °C (N-S), whereas mean soil-surface temperatures were 14.43 and 13.31 °C, respectively. On a representative cloudy day, daytime soil-surface temperature was 2.48 °C lower in the N-S block. The CFD model reproduced broad surface-temperature cycles on both representative days; canopy-air comparison was restricted to the sunny day from 12:30 to 21:00. Under the tested operating conditions, layout-related contrasts were more evident at the soil surface than in mean canopy air. Because the comparison involved two unreplicated blocks within one greenhouse and did not include crop-response measurements, these findings should be interpreted as exploratory thermal associations rather than evidence of a general causal or agronomic advantage of either ridge orientation.

Keywords: Chinese solar greenhouse; tomato; ridge layout; canopy-air temperature; soil-surface storage; solar geometry; CFD

Check for updates

Academic Editor: Zhi Huang

Received: 4 September 2026
Revised: 15 October 2026
Accepted: 21 October 2026
Published: 26 October 2026

Copyright: © 2026 by the authors. Licensee MDPI, Basel, Switzerland. This article is an open access article distributed under the terms and conditions of the Creative Commons Attribution (CC BY) license.

1. Introduction

Winter vegetable production in northern China depends on protected structures that can maintain a suitable crop environment through large day–night temperature swings. Chinese solar greenhouses (CSGs) address this challenge through a south-facing transparent cover, a massive north wall, and movable night insulation, enabling winter production with limited active heating [1–4]. Their performance therefore depends on how solar energy enters the enclosure, how heat is stored in the soil and walls, and how that heat is released over day and night. Understanding these processes is important for improving greenhouse operation under cold-season conditions, when small differences in heat storage and surface exposure can shape the local crop environment [5].

The greenhouse microclimate is spatially heterogeneous. Short-wave radiation, long-wave exchange, conduction through the soil and enclosure, ventilation, and crop-canopy transpiration act together to produce local temperature gradients [6–9]. Air temperature is widely used as a summary indicator, but it does not fully describe the thermal conditions experienced by plants. A greenhouse-wide mean can conceal differences between exposed and shaded locations, while soil surface and enclosure-surface temperatures provide information about heat storage and the thermal boundary of the root zone [10]. Evidence from controlled experiments also shows that sufficiently low root-zone temperatures can affect tomato photosynthesis, root development, and mineral acquisition [11]. However, whether these crop-level responses apply to the smaller temperature differences typically found between ridge-layout comparisons remains uncertain. This uncertainty is one reason why canopy-air temperature alone is an incomplete description of the crop thermal environment.

Ridge and row orientation is one practical factor that can modify this environment. N-S ridges change the timing and distribution of inter-row shading as the sun moves across the greenhouse, whereas E-W ridges produce a different relationship between row surfaces, the south-facing cover, and the north wall. Orientation also affects the space available for transport, spraying, harvesting, and automated navigation. Previous studies have shown that row direction changes the uniformity of light absorption within tomato canopies [12], while its implications for whole-canopy photosynthesis remain less clear. Crop-row corridors also influence the operation of greenhouse robots [13,14]. Thus, ridge orientation has both a microclimatic and an operational dimension. The relevant question is not simply which orientation is warmer, but where the thermal contrast occurs and how it changes with solar exposure and weather.

Existing greenhouse studies have used field measurements, energy-balance analysis, and computational fluid dynamics (CFD) to examine temperature, radiation, airflow, and heat storage. A recent CFD study examined the influence of tomato crop-row orientation on the microclimate of a Chinese solar greenhouse [15]. Measurements provide direct evidence of the thermal response at selected locations, whereas CFD can resolve the spatial pattern between sensors and test whether a measured contrast is consistent with the underlying heat-transfer processes [16,17]. CFD is therefore most useful when it is evaluated against observations and used to interpret spatial mechanisms, rather than treated as a replacement for field measurements.

Despite this progress, few studies have directly compared E-W and N-S ridge layouts within the same operating Chinese solar greenhouse under the same outdoor forcing, using both distributed temperature measurements and a spatially resolved CFD model. In particular, it remains unclear whether the layout-related contrast is expressed mainly in canopy air or in the soil surface and enclosure surfaces, and whether the contrast changes between sunny and cloudy conditions. Addressing this gap requires a comparison that keeps the greenhouse context and general weather exposure comparable while examining several components of the thermal environment.

In this study, we conduct an exploratory operational case study of microclimate organization in a real-world Chinese solar greenhouse by comparing E-W and N-S tomato ridge-layout blocks during an early-winter observation period. We combine measurements of canopy-air, soil-surface, plastic-film, north-wall, and rear-slope temperatures with solar-geometry calculations and transient CFD simulations. The study examines whether layout-related thermal contrasts are more evident at heat-storage and enclosure surfaces than in mean canopy air and whether these contrasts change between sunny and cloudy conditions. The purpose is to characterize the observed thermal organization under actual greenhouse operating conditions and to use CFD to interpret its spatial patterns, rather than to establish a universal or greenhouse-wide causal effect of ridge orientation. Because the experiment

was conducted in one greenhouse without independent layout replication or crop-level measurements, the findings should be interpreted as exploratory thermal associations that require confirmation in replicated multi-greenhouse and crop-response studies.

Figure 1 summarizes the analytical framework. The E-W and N-S ridge-layout blocks were separated by a thin-film partition in both the field experiment and CFD geometry to limit direct air exchange. The ridge layout was treated as an operational configuration acting with weather through radiative exposure and shading, airflow, and heat storage in the soil surface and enclosure. Continuous measurements provided temporal evidence at defined locations, whereas CFD was used to examine spatial coherence around the measurement locations. The framework separates observed between-block thermal contrasts from crop and management effects that remain to be tested.

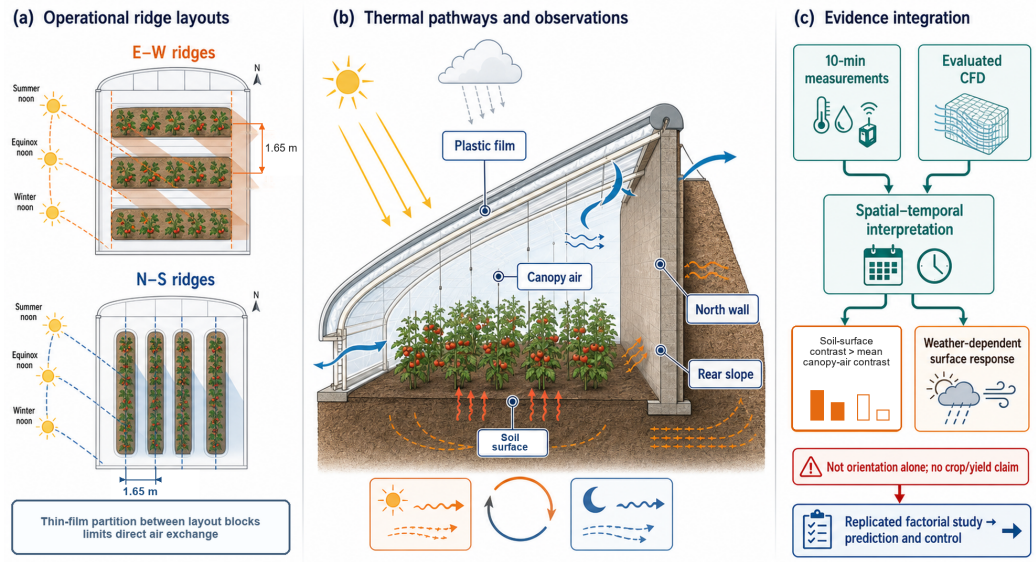


Figure 1. Conceptual and analytical framework of the study. (**a**) Operational E-W and N-S ridge layouts; orange and blue dashed solar paths indicate the seasonal solar positions considered for the two layouts, and the dimension arrows indicate the 1.65 m ridge centre-to-centre spacing. (**b**) Thermal pathways and observation locations; yellow arrows indicate incoming solar radiation, blue arrows indicate ventilation and air movement, orange/red arrows indicate heat transfer and thermal storage in the soil and enclosure, and the sun/cloud icons distinguish sunny and cloudy conditions. (**c**) Evidence integration; teal boxes show measurements, CFD, and spatial–temporal interpretation, orange boxes show the principal thermal comparisons, the red box states the interpretation boundary, and the blue box indicates the need for replicated studies. The thin-film partition between layout blocks limits direct air exchange.

2. Materials and Methods

2.1. Experimental Greenhouse and Ridge-Layout Configurations

We conducted the experiment in greenhouse No. 48 at the Houshan Experimental Base of Shenyang Agricultural University, Shenyang, Liaoning Province, China. The greenhouse long axis was approximately east–west, and the light-transmitting plastic cover faced south. The greenhouse was approximately 8 m wide and 60 m long, with a ridge height of 4.6 m and a north-wall height of 3.2 m. We grew winter tomato (*Solanum lycopersicum* L.) in raised ridges under two operational configurations: E-W ridges parallel to the greenhouse long axis and N-S ridges across the greenhouse span. Each ridge contained two crop rows separated by 0.30 m, and ridge center lines were spaced 1.65 m apart in both layouts. The E-W and N-S ridges were 10.0 and 6.4 m long, respectively, and a 1.50 m clear passage separated the two layout blocks. A thin-film partition was installed within this passage throughout the monitoring period to limit direct air exchange between the

blocks. The plants formed a continuous crop canopy with a measured height of 1.60 m during the observation period. Figures 2 and 3 show the greenhouse and the two ridge-layout configurations. We based all analyses and figures on observations collected from 22 November to 3 December 2025.



Figure 2. Experimental Chinese solar greenhouse in Shenyang, China.



(**a**) (**b**)

Figure 3. Tomato ridge-layout configurations: (**a**) N-S ridges and (**b**) E-W ridges.

Each crop row had one drip line, with each emitter corresponding to one substrate bag and positioned between adjacent plant roots. On sunny days, the reported irrigation schedule was 100 mL per plant at 08:00, 11:00, and 13:00; no irrigation was applied on cloudy days. The insulation blanket was opened at 09:00 and closed at 16:00. When indoor temperature exceeded 30 °C on sunny days, the upper vent was opened by approximately 20 cm for about 15 min on average; otherwise, the greenhouse remained closed. These operating rules were shared by both blocks. Event-level irrigation delivery and vent flow were not continuously recorded.

2.2. Sensor Layout and Measured Variables

Measured variables comprised outdoor air temperature; canopy-air temperature at 1 m height at film-side, middle, and north-wall-side positions; and soil-surface, plastic-film, rear-slope, and rear-wall surface temperatures. The soil-surface probes were placed at the exposed surface between crop rows, not at multiple depths in the active root zone.

Soil-surface temperature therefore describes the measured surface condition and is not a depth-resolved root-zone temperature. Film and enclosure temperatures described surface heating and cooling [18,19]. Table 1 summarizes the measured variables. White testo 174H temperature–humidity data loggers (Testo SE & Co. KGaA, Titisee-Neustadt, Germany) recorded outdoor and canopy-air temperatures; black testo 176T4 temperature data loggers with external probes (Testo SE & Co. KGaA, Titisee-Neustadt, Germany)recorded surface temperatures. In the E-W block, the three canopy-air loggers were placed on the second crop row of the first, second, and fourth ridges at 6.20, 4.55, and 1.25 m from the north-wall datum, respectively. The corresponding soil-surface sensor near the first logger was at 6.10 m from that datum. Corresponding N-S sensors were aligned with the E-W transect at comparable positions across the greenhouse span. All sensors were placed away from the thin-film partition, as shown in Figure 4. Examples of the temperature sensor installations are shown in Figure 5. These were location-specific measurements, not independent replicated observations.

Table 1. Measured temperature variables and their use in this study.

Variable Category	Measurement Object	Orientation	Use in This Study
Outdoor air temperature	Air outside the greenhouse	Common boundary	Identifying outdoor low-temperature variation and weather processes
Canopy-air temperature	Film-side, middle and north-wall positions at 1 m height	E-W and N-S	Comparing crop-zone air temperature and spatial uniformity
Soil-surface temperature	Soil surface between crop rows near the plastic-film side	E-W and N-S	Describing local soil-surface temperature, not a depth-resolved root-zone profile
Plastic-film temperature	South plastic-film surface or nearby position	E-W and N-S	Evaluating film-side radiative heating and envelope thermal response
Rear-slope/rear-wall temperature	Rear-slope and rear-wall surfaces near the north wall	E-W and N-S	Interpreting heat absorption and release by thermal-storage structures

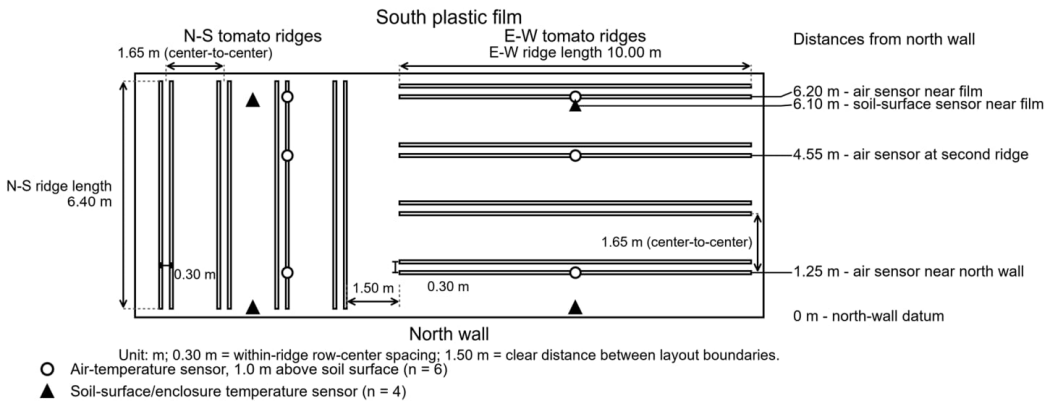


Figure 4. Experimental layout of the E-W and N-S tomato ridges and temperature sensors. Ridge spacing was measured center to center; each ridge contained two crop rows separated by 0.30 m. The thin-film partition limited direct air exchange between the blocks. Circles denote 1 m canopy-air sensors; triangles denote soil-surface or enclosure-surface sensors.



(**a**) (**b**) (**c**)

Figure 5. Examples of (**a**) plastic-film, (**b**) soil-surface, north-wall/rear-slope, and (**c**) 1 m canopy-air temperature measurements.

2.3. Data Processing and Evaluation Indices

Raw records were organized as unified time series at 10 min intervals. The daytime period was defined as 08:00–16:00; all other times were treated as non-daytime. For each day, we calculated the mean, maximum, minimum, diurnal range, and daytime mean temperature. At each time point, the canopy-air spatial range was the difference between the maximum and minimum among the three 1 m·sensors within a layout. The daytime mean spatial range was the mean of this quantity across all daytime records. The coefficient of variation (CV), calculated as the standard deviation divided by the mean of the three air-temperature measurements, described the canopy-air uniformity.

Quality control preceded descriptive analysis. The audit covered 53,808 long-format records from 46 sensor channels, and the common analysis window was restricted to overlapping valid channels at 10 min resolution. Duplicate timestamps and missing intervals were documented without interpolation. Each representative day contained 144 records per valid channel.

The full 12-day record was used for descriptive statistics. We chose 28 November 2025 and 30 November 2025 for detailed time-resolved CFD comparison because they showed contrasting observed weather and greenhouse thermal responses, as well as clear between-block differences. On 28 November, the outdoor diurnal temperature range was 15.50 °C, and the soil surface, film, and canopy air warmed strongly. The observed weather on 30 November was cloudy, with much weaker indoor surface and canopy-air warming; the daytime between-block soil-surface difference reached 2.48 °C. We use the terms sunny response and cloudy response to describe these observed conditions, not measured irradiance classes. Global solar radiation and photosynthetically active radiation were not measured, and selection for a pronounced contrast does not make these days statistically representative of the entire monitoring period.

2.4. Solar-Geometry Calculation and Potential Inter-Row Shading Interpretation

Because solar radiation was not measured, irradiance was not used as an observed evaluation variable. Instead, solar elevation and azimuth were calculated from site coordinates, date, and time using established solar-position formulations [20,21]. Declination and extraterrestrial solar geometry followed standard astronomical and solar-engineering treatments [22–24]. The calculations described potential illumination and shading differences between E-W and N-S ridges at low solar altitude (Figure 6). The site was located at 41.8° N, 123.6° E, and all calculations used Beijing time (UTC+8).

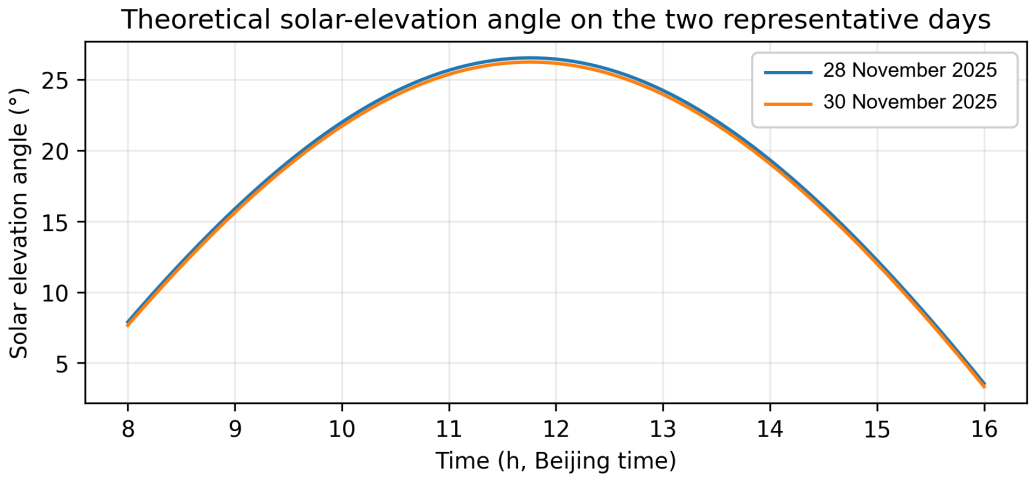


Figure 6. Theoretical solar-elevation angles on sunny and cloudy response days. The two curves were nearly superimposed.

The solar-elevation angle h_s was calculated as follows:

$$\sin(h_s) = \sin(\varphi)\sin(\delta) + \cos(\varphi)\cos(\delta)\cos(\omega). \quad (1)$$

where φ is latitude, δ is solar declination, and ω is solar hour angle. Solar declination was approximated as $\delta = 23.45 \sin[360(284 + n)/365]$, where n is the day of year. With the measured tomato canopy height H_c of 1.6 m, the potential horizontal shadow length was estimated as:

$$L_s = H_c/\tan(h_s) \quad (2)$$

For each ridge orientation, the component perpendicular to the crop rows was considered when interpreting potential inter-row shading. This geometric interpretation did not represent measured radiation.

Both layouts had a ridge center-to-center spacing of 1.65 m; each ridge contained two crop rows separated by 0.30 m, and the measured tomato canopy height was 1.60 m. The E-W and N-S ridge lengths were 10.0 and 6.4 m, respectively. These parameters were used in the solar-geometry and potential-shading interpretation.

2.5. CFD Model and Evaluation Against Measurements

The CFD model was compared with measured temperature series from the sunny-response day (28 November) and cloudy-response day (30 November). Soil-surface, north-wall, and rear-slope temperatures were compared on both days. Canopy-air temperature was compared only on sunny days, from 12:30 to 21:00. Figures 7 and 8 show the model geometry and comparison workflow.

The model included the plastic cover, north wall, rear slope, side walls, a 1.0 m·soil layer, simplified tomato canopy solid regions, and a thin-film partition in the 1.50 m passage separating the E-W and N-S blocks. The E-W and N-S layouts followed the field arrangement. Each ridge contained two crop rows separated by 0.30 m, and ridge center lines were spaced 1.65 m apart in both layouts. The canopy was represented as a continuous 1.60 m-high solid region. Model inputs and thermophysical properties are listed in Tables 2 and 3.

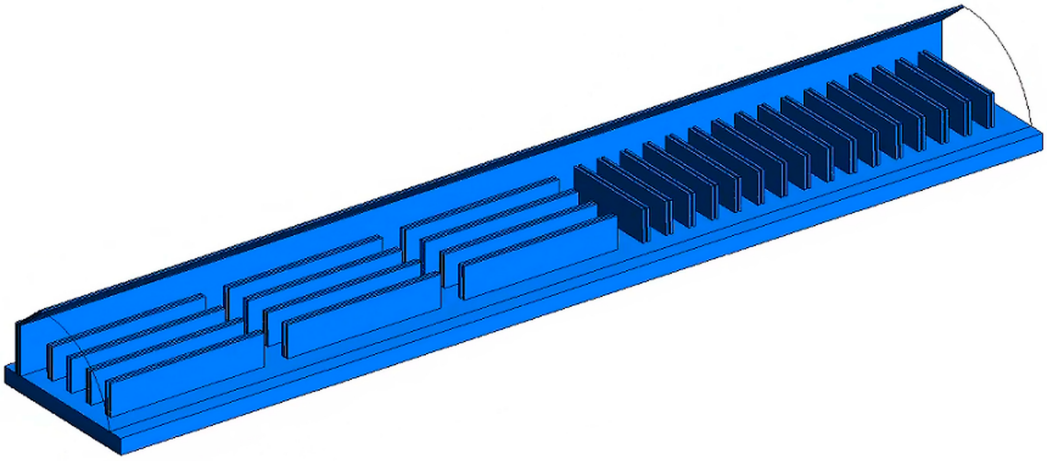


Figure 7. CFD geometry of the solar greenhouse and simplified tomato canopy blocks.

Table 2. CFD model inputs and measured comparison variables.

Boundary	Model Treatment	Primary Basis	Role in Comparison
Outdoor environment	External thermal boundary	Measured representative-day outdoor temperature	Environmental driver
Plastic cover	Conjugate heat transfer and radiative wall	Material and structural properties	Model input
soil	Conjugate solid region	Soil properties and initial thermal state	Compared with measured soil-surface temperature
North wall	Conjugate solid region	Wall materials and geometry	Compared with measured rear-wall temperature
Rear slope	Conjugate solid region	Rear-slope materials and geometry	Compared with measured rear-slope temperature
Tomato canopy	Simplified 1.6 m canopy solid region	Measured row orientation, spacing and canopy height	Compared with measured canopy air
Solar radiation	Solar Calculator and ray tracing	41.8° N, 123.6° E, UTC+8 and date	Calculated input
Crop-zone air	Six sampling points at 1 m height	Sensor locations under both orientations	Core comparison variable

Table 3. Thermophysical properties used in the CFD model.

Material	Density ($kg \cdot m^{-3}$)	Specific Heat ($J \cdot kg^{-1} \cdot K^{-1}$)	Conductivity ($W \cdot m^{-1} \cdot K^{-1}$)	Model Role
Air/air-crop fluid	1.225	1006.43	0.0242	Dynamic viscosity = 1.7894×10^{-5} Pa·s
Plastic film	927	2118	0.200	Solid cover material
Soil	1800	1250	1.180	1.0 m thermal-storage layer
Tomato-crop solid	560	2100	0.190	Simplified canopy solid region
Masonry block	2100	840	1.400	North-wall layer
Insulation quilt	50	1000	0.050	Night insulation layer
EPS	50	880	0.027	Insulation layer
Cement	2300	880	1.500	Rear-slope/wall layer
Wood	650	1200	0.140	Rear-slope layer

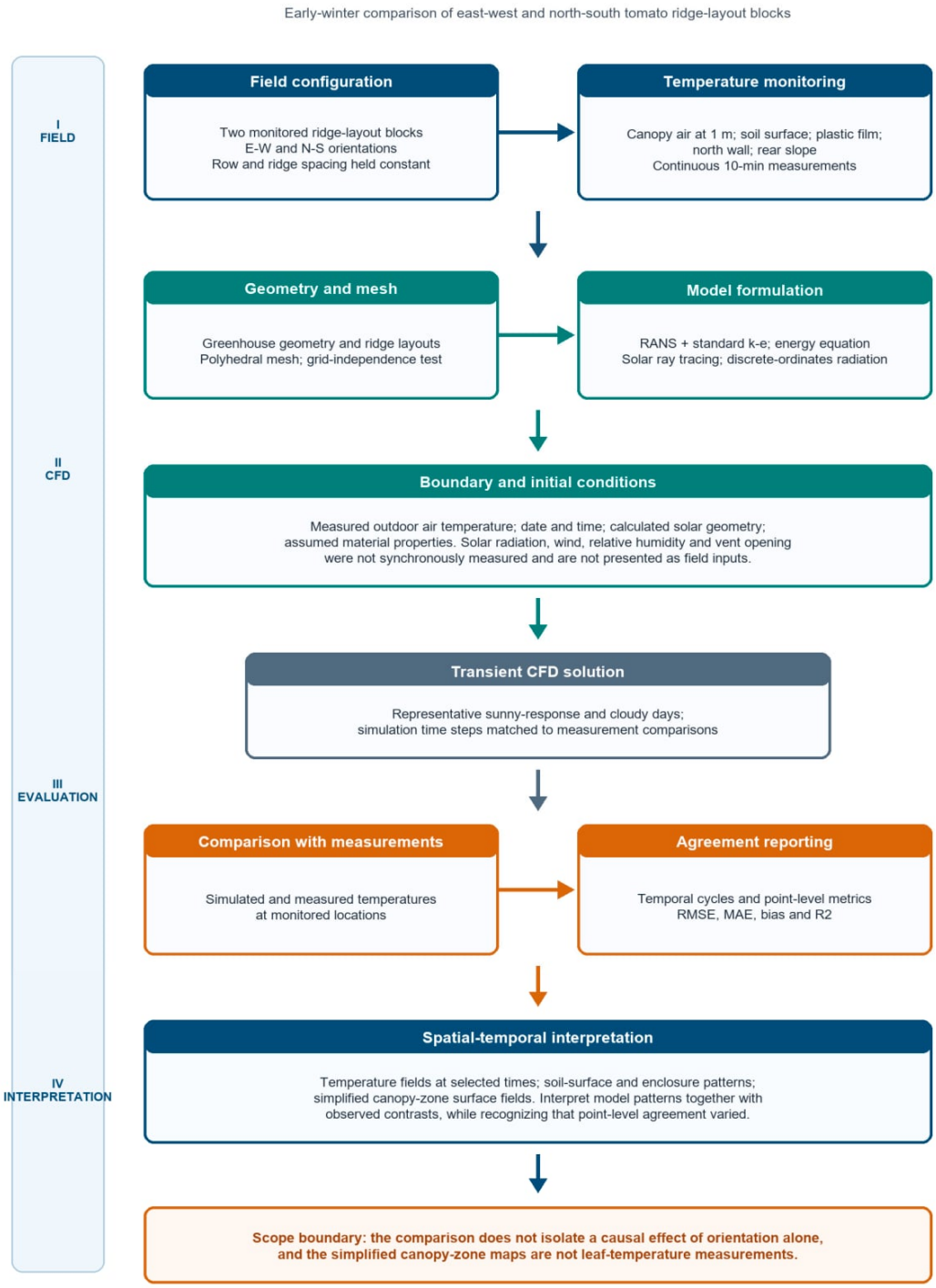


Figure 8. Workflow for field monitoring, CFD modeling, and evaluation against measurements.

CFD simulations were performed using ANSYS Fluent 2023 R1 (ANSYS, Inc., Canonsburg, PA, USA). We used a three-dimensional, double-precision, pressure-based transient solver with energy, the standard k-ε turbulence model and standard wall functions, solar ray tracing, and discrete-ordinates radiation. Each simulation used a 1800 s time step, a maximum of 20 iterations per step, and 48 half-hour outputs (Table 4). The journals did not specify normalized-residual stopping thresholds. A retrospective check at iteration 20 against reference levels of 10^{-3} for continuity, momentum, k, and ε and 10^{-6} for energy found that 44 of 48 steps on each day met all reference levels; the first four did not. Thus, convergence cannot be confirmed for every step. Air density was fixed at 1.225 kg·m^{-3}, so buoyancy-driven natural convection was not explicitly resolved. The formulation was

informed by agricultural CFD studies [25–27], and numerical implementation followed the ANSYS Fluent Theory Guide [28]. The thermophysical and optical properties in Table 3 were nominal literature-based inputs rather than measurements of greenhouse No. 48; their uncertainty limits point-level interpretation.

Table 4. CFD mesh and principal numerical settings.

Item	Final Setting
Solver	3D, double precision, pressure-based, transient
Mesh	313,829 polyhedral cells; 9 cell zones; 1,550,085 nodes
Energy	Enabled
Turbulence	Standard k-ε model
Radiation	Discrete Ordinates plus Solar Ray Tracing/ Solar Calculator
Gravity	(0, −9.8, 0) m·s^{-2}
Air density	Constant, 1.225 kg·m^{-3}
Pressure-velocity coupling	Coupled
Pressure interpolation	PRESTO!
Momentum, k, ε	First-order upwind
Energy	Second-order upwind
Physical time step	1800 s
Iterations per time step	20
Simulated duration	86,400 s; 48 half-hour solution levels
Operating pressure	101,325 Pa

Both ridge layouts were simulated for the two representative days. Measured outdoor temperature provided the external thermal driver, while the field geometry, thin-film partition, material properties, and solar geometry were represented in the model. Ventilation was approximated by a temperature-triggered condition when indoor temperature exceeded 30.00 °C. The exact vent opening and closing times, airflow rate, wind-driven exchange, irrigation-related soil-moisture changes, and insulation state were not recorded at the simulation time-step resolution. The model therefore did not resolve every short ventilation or irrigation event. Simulated temperatures were sampled at the measured soil-surface, north-wall, rear-slope, and 1 m canopy-air positions. Greenhouse models are sensitive to ventilation assumptions [29–32].

Agreement was described using root mean square error (RMSE), mean absolute error (MAE), mean bias, and the coefficient of determination (R^2). RMSE and MAE were the primary absolute-error indicators; R^2 was interpreted cautiously when the measured temperature range was narrow. The surface comparison covered six soil-surface, north-wall, and rear-slope locations on both days, whereas the six-location canopy-air comparison covered only 12:30–21:00 on the sunny day. These same-period comparisons assess reproduced temporal patterns but are not independent external validation.

The production mesh contained 313,829 polyhedral cells. A sensitivity assessment at 12:30 on 28 November compared this mesh with meshes of 1,135,080 and 3,454,016 cells (Table 5; Figure 9). Medium-to-fine differences were small at the six canopy-air points but larger and non-monotonic at several surface points. This mesh dependence was taken into account when interpreting the surface results [33–36].

A retrospective Fluent wall Y+ check of saved representative-day states gave area-weighted means of 0.010 at the crop interface, 0.020 at the plastic cover, 0.0097 at the inner north-wall surface, and 0.014 at the soil-side interface; the maximum on these selected boundaries was 1.61. The mesh passed a global grid check, but first-cell heights and a dedicated near-wall resolution assessment were unavailable. These Y+ values cannot establish adequate boundary-layer treatment with standard wall functions.

Table 5. Mesh-sensitivity analysis at 12:30 on 28 November 2025.

Quantity	Production	Medium	Fine	Interpretation
Cell count	313,829	1,135,080	3,454,016	Local adaptation around the representative E-W and N-S monitoring segment.
Nominal refinement ratio	—	1.535	1.449	Computed from cell-count ratios to describe the local refinement sequence.
Mean of all 12 monitoring points (°C)	22.795	22.096	21.575	Mean absolute fine-minus-medium difference = 0.592 °C.
Mean of six canopy-air points (°C)	19.457	19.365	19.433	Mean/max absolute fine-minus-medium difference = 0.073/0.394 °C.
Mean of six surface points (°C)	26.133	24.827	23.717	Mean/max absolute fine-minus-medium difference = 1.111/1.807 °C.
Interpretation	Production grid	Refined grid	Fine local grid	Canopy-air comparison was robust; surface points were more mesh-sensitive and did not satisfy monotonic GCI assumptions.

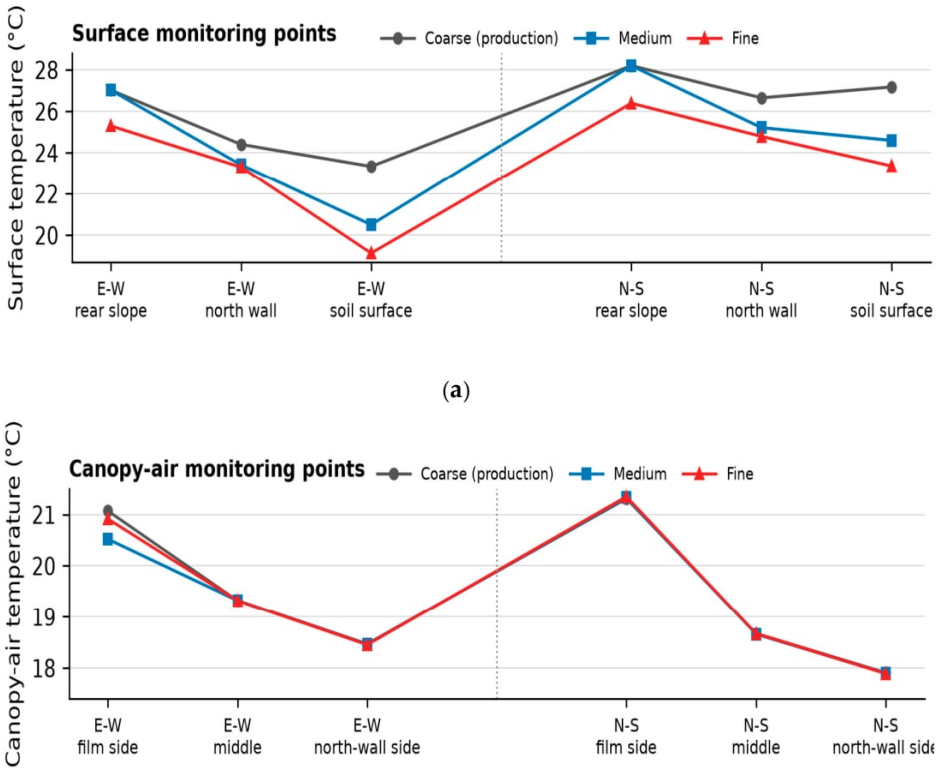


Figure 9. Mesh-sensitivity comparison at (**a**) six surface and (**b**) six canopy-air locations at the representative time.

During post-processing, each half-hour solution was assigned its physical time. Identical sampling locations and performance metrics were used for the E-W and N-S cases. The

Solar Calculator supplied the time-varying solar direction, and the soil surface, enclosure, and canopy were analyzed as separate thermal regions.

3. Results

3.1. Overall Temperature Variation During the Observation Period

Outdoor and indoor temperatures varied markedly from 22 November to 3 December 2025. Mean canopy-air temperatures were similar between E-W and N-S ridges, whereas soil-surface, plastic-film, north-wall, and rear-slope temperatures showed clearer layout-related differences (Figure 10).

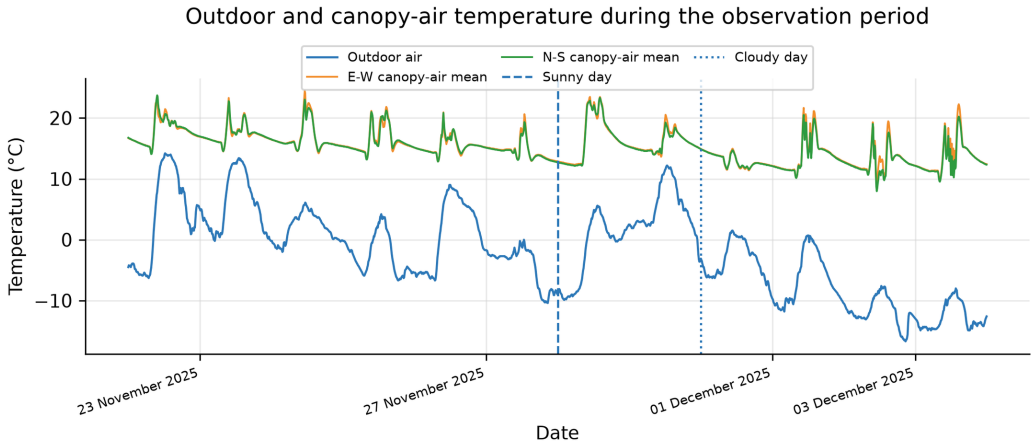


Figure 10. Outdoor air temperature and mean canopy-air temperature under E-W and N-S ridges during the observation period from 22 November to 3 December 2025.

Across the observation period, mean canopy-air temperatures were 15.34 °C under E-W ridges and 15.22 °C under N-S ridges, a difference of 0.12 °C. Mean soil-surface temperatures were 14.43 and 13.31 °C, respectively, a difference of 1.12 °C. The between-layout difference was therefore greater for soil-surface temperature than for mean canopy-air temperature (Figure 11).

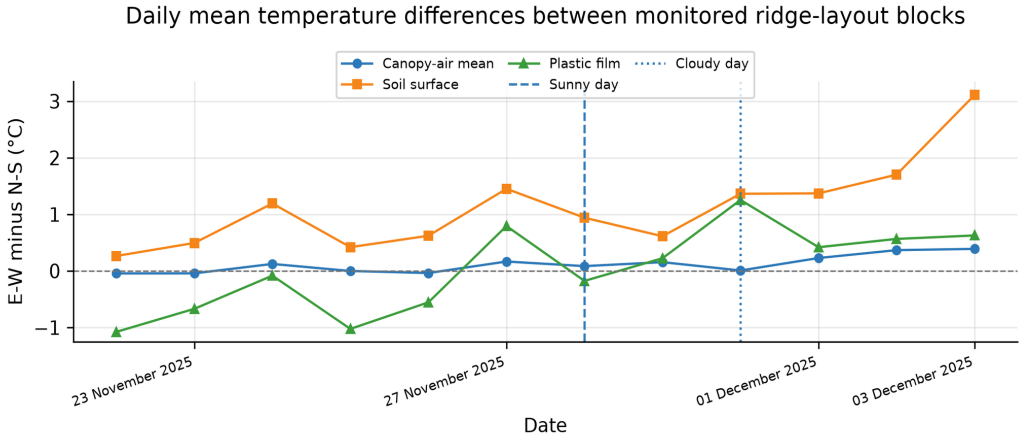


Figure 11. Daily mean temperature differences between monitored E-W and N-S ridge-layout blocks during the observation period. Positive values indicate that the E-W block was warmer than the N-S block. The gray dashed horizontal line indicates zero difference (E-W minus N-S = 0 °C).

3.2. Selection of Representative Response Days

Daily patterns were identified on 28 November 2025 as the sunny-response day and on 30 November as the cloudy-response day. On 28 November, the outdoor maximum and minimum were 5.60 and −9.90 °C, giving a range of 15.50 °C, and the soil surface, film,

and canopy air warmed strongly. On 30 November, the outdoor maximum and minimum were 1.50 and −9.50 °C. Although the outdoor range was 11.00 °C, the canopy-air range was only 3.90–4.30 °C and soil-surface and film warming were weak (Table 6). The selected days illustrate contrasting observed responses rather than the distribution of all 12 days.

Table 6. Representative response days and outdoor temperature characteristics.

Date	Response Class	Selection Basis	Outdoor Mean	Outdoor Max.	Outdoor Min.	Outdoor Range
28 November 2025	Sunny response	Large outdoor diurnal range and clear warming of soil surface, film, and rear‘slope	−2.05	5.60	−9.90	15.50
30 November 2025	Cloudy response	Small canopy-air diurnal range and weak soil-surface and film warming	−3.42	1.50	−9.50	11.00

3.3. Temperature Response on the Sunny-Response Representative Day

On 28 November, canopy-air temperature under both layouts followed a clear diurnal cycle. Daily and daytime means were 16.53 and 20.36 °C under E-W ridges and 16.44 and 20.20 °C under N-S ridges. The maximum among the three air sensors was approximately 24.30 °C for both layouts (Figure 12).

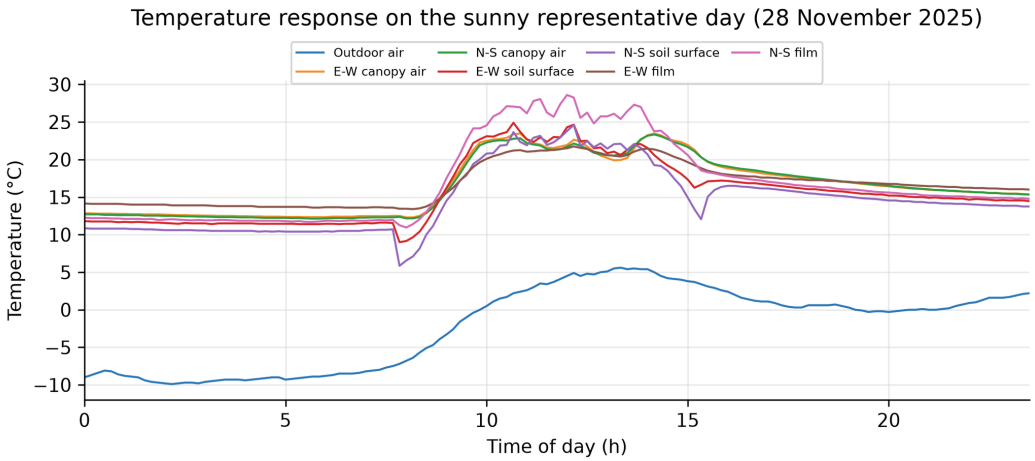


Figure 12. Diurnal temperature response on the sunny-response representative day (28 November 2025).

The main sunny-day contrasts occurred at the soil surface, plastic film, and north wall. Daytime mean soil-surface temperature was 19.79 °C under E-W ridges and 18.61 °C under N-S ridges. Conversely, the N-S film had a daytime mean of 22.79 °C and a maximum of 28.60 °C, compared with 19.40 and 21.75 °C under E-W ridges. The N-S north wall was also warmer during the day, whereas the E-W rear slope was slightly warmer.

3.4. Temperature Response on the Cloudy Response Day

On 30 November, the amplitude of indoor temperature variation decreased substantially. Daily mean canopy-air temperature was 13.03 °C under both layouts, and daytime means were 12.62 °C under E-W ridges and 12.67 °C under N-S ridges. Consequently, mean canopy-air temperature differed little between layouts on this day (Figure 13).

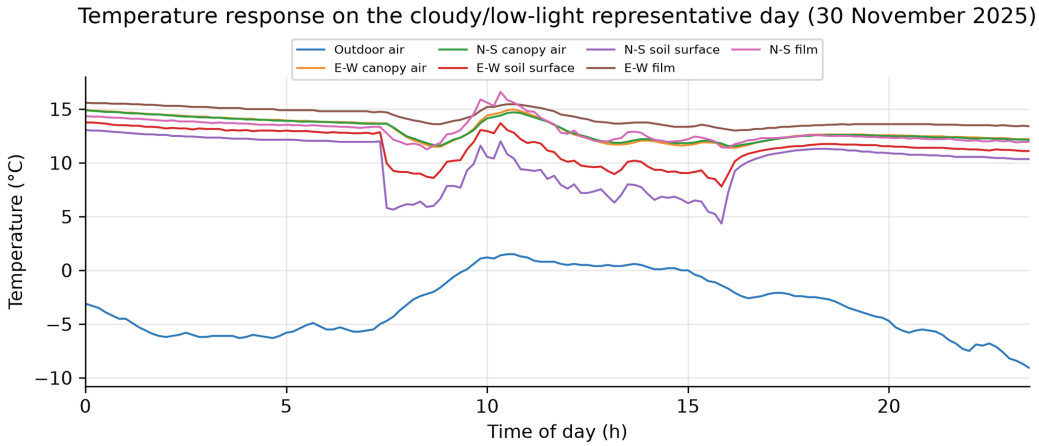


Figure 13. Diurnal temperature response on the cloudy response day (30 November 2025).

Soil-surface temperature differences remained pronounced under cloudy conditions. Daytime mean soil-surface temperature was 10.23 °C under E-W ridges and 7.75 °C under N-S ridges, a difference of 2.48 °C. The N-S soil surface was colder when solar forcing was weak. Root activity and water or nutrient uptake were not measured, so the crop response to this soil-surface temperature difference is unknown.

3.5. Spatial Uniformity of Canopy-Air Temperature

Canopy-air spatial range was calculated from the film-side, middle, and north-wall sensors within each layout. During sunny daytime, mean spatial ranges were 1.76 °C under E-W ridges and 1.73 °C under N-S ridges. The corresponding maximum ranges were 2.80 and 3.40 °C. Under cloudy conditions, daytime mean ranges fell to 0.53 °C under E-W ridges and 0.31 °C under N-S ridges. Maximum ranges also fell to 0.90 and 0.70 °C, respectively. Spatial variation in canopy-air temperature was therefore smaller on cloudy days (Table 7; Figure 14).

Table 7. Canopy-air temperature and spatial uniformity under representative response conditions.

Date	Response Class	Layout	Daily Mean	Daytime Mean	Maximum	Range	Mean Spatial Range	Max. Spatial Range	Daytime CV (%)
28 November 2025	Sunny	E-W	16.53	20.36	24.30	12.50	1.76	2.80	3.72
28 November 2025	Sunny	N-S	16.44	20.20	24.30	12.50	1.73	3.40	3.79
30 November 2025	Cloudy	E-W	13.03	12.62	15.30	4.30	0.53	0.90	1.81
30 November 2025	Cloudy	N-S	13.03	12.67	15.20	3.90	0.31	0.70	1.09

3.6. Soil-Surface, Plastic-Film, and Thermal-Storage Structure Temperatures

Soil-surface and film temperatures showed contrasting patterns between layouts. On the sunny day, E-W ridges maintained a warmer soil surface, whereas N-S ridges produced higher film temperatures. Under cloudy conditions, the E-W soil-surface temperature advantage increased, and the sunny-day N-S film advantage disappeared. The N-S north wall was warmer during the sunny daytime, while wall temperatures were similar between layouts under cloudy conditions (Table 8).

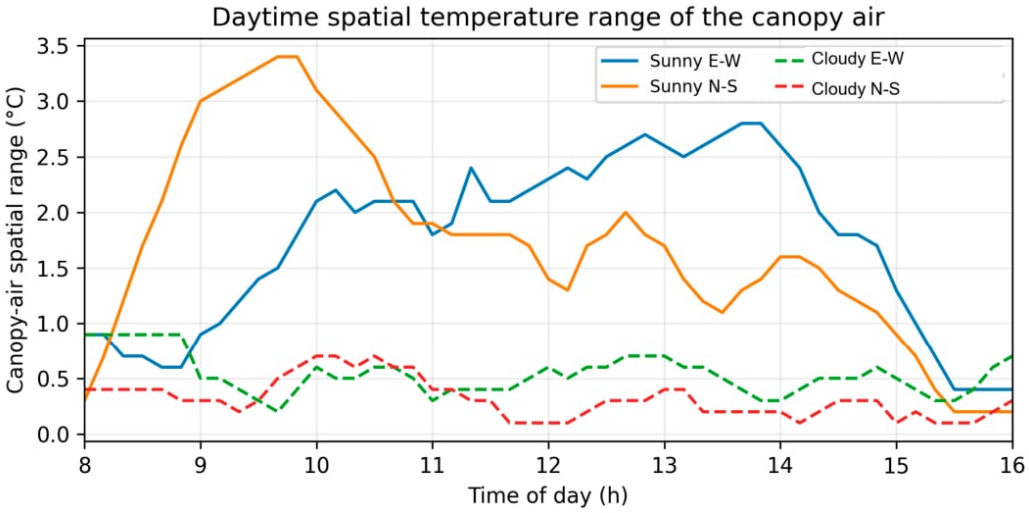


Figure 14. Daytime spatial range of canopy-air temperature on the representative response days. The spatial range is the difference between the maximum and minimum values among the three canopy-air sensors under the same orientation.

Table 8. Soil-surface, plastic-film, and heat-storage-structure temperatures under representative conditions (°C).

Date	Response Class	Layout	Soil-Surface Daily Mean	Soil-Surface Daytime Mean	Soil-Surface Max.	Film Daytime Mean	Film Max.	Wall Daily Mean	Rear-Slope Daily Mean
28 November 2025	Sunny	E-W	15.58	19.79	24.90	19.40	21.75	18.73	18.06
28 November 2025	Sunny	N-S	14.64	18.61	24.60	22.79	28.60	19.72	17.86
30 November 2025	Cloudy	E-W	11.48	10.23	13.75	14.12	15.60	14.78	13.35
30 November 2025	Cloudy	N-S	10.11	7.75	13.05	13.03	16.60	14.90	13.31

3.7. Integrated Interpretation Using Solar Geometry and CFD

Theoretical solar-elevation curves were similar on 28 and 30 November 2025. Maximum solar elevations near noon were approximately 26.5° and 26.2°, and the corresponding minimum horizontal shadow lengths were approximately 3.21 and 3.25 m. The small geometric difference did not match the large difference in thermal response between days. Radiation was not measured, so the effects of cloud cover and atmospheric transmittance could not be separated from greenhouse heat storage.

CFD converted the solar direction, greenhouse geometry, and crop-row arrangement into three-dimensional temperature fields. The resulting soil-surface, enclosure, and canopy-air fields were compared with measurements to assess temporal consistency and spatial organization. The comparison therefore examined whether the model reproduced the measured response at the monitored locations and whether the measurement-compared fields could support spatial interpretation.

3.8. CFD Comparison with Measured Surface Temperatures

CFD and measurements were compared at six soil-surface, north-wall, and rear-slope positions on both representative days (Table 9; Figures 15 and 16). Sunny-day soil-surface RMSE was 1.56 °C in the E-W block and 2.97 °C in the N-S block. The larger N-S error may reflect rapidly changing inter-row shading that the simplified continuous canopy cannot resolve. On the cloudy day, surface RMSE values ranged from 0.46 to 0.94 °C, but the E-W soil-surface R^2 was −0.33. Because the observed cloudy series varied little, a modest

absolute error can yield a negative R^2; RMSE and MAE are more informative for this case. The model reproduced broad cycles, but its point-level agreement varied, particularly with local shading and low temperature variation. It is used here to interpret spatial patterns rather than provide exact point predictions.

Table 9. CFD-measurement comparison statistics at six surface locations.

Condition	Position	RMSE (°C)	MAE (°C)	Bias (°C)	R^2
Sunny	E-W soil surface	1.56	1.18	0.70	0.86
Sunny	N-S soil surface	2.97	2.08	1.73	0.51
Sunny	E-W wall	1.98	1.70	0.16	0.81
Sunny	N-S wall	2.05	1.66	0.87	0.80
Sunny	E-W slope	1.23	0.91	−0.73	0.95
Sunny	N-S slope	1.17	0.92	−0.27	0.95
Cloudy	E-W soil surface	0.94	0.86	−0.86	−0.33
Cloudy	N-S soil surface	0.80	0.76	−0.68	0.38
Cloudy	E-W wall	0.46	0.38	−0.25	0.78
Cloudy	N-S wall	0.59	0.51	−0.37	0.64
Cloudy	E-W slope	0.81	0.66	0.23	0.29
Cloudy	N-S slope	0.90	0.76	0.13	0.16

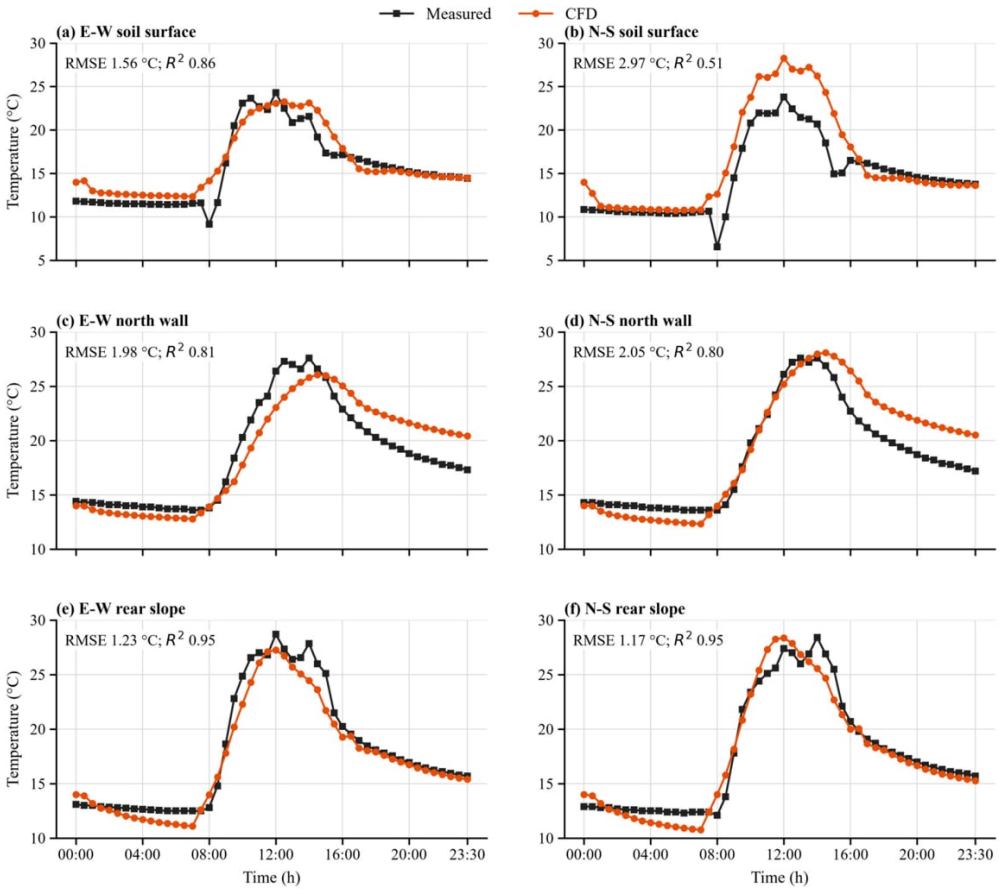


Figure 15. Measured and CFD-simulated temperatures at six positions on 28 November 2025.

3.9. CFD Comparison with Canopy-Air Temperature

For the sunny case, CFD was compared with 108 paired measurements at six canopy-air locations from 12:30 to 21:00. Overall RMSE was 1.52 °C, MAE was 1.36 °C, mean bias was +0.69 °C, and R^2 was 0.564 (Table 10; Figure 17). The E-W middle location had the largest RMSE (1.83 °C). The positive bias indicates modest overprediction during part of the comparison period.

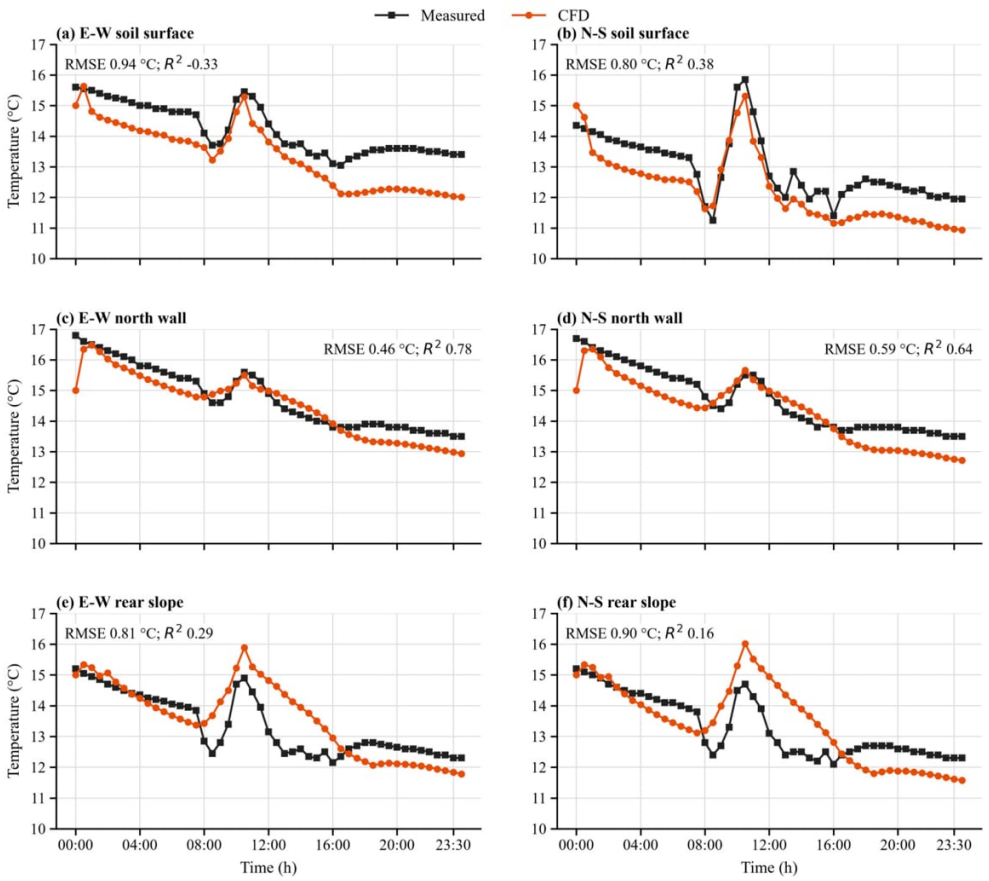


Figure 16. Measured and CFD-simulated soil-surface, north-wall, and rear-slope temperatures on a cloudy-response day (30 November 2025).

Table 10. CFD-measurement comparison metrics for canopy-air temperature under sunny conditions.

Location	n	MAE (°C)	RMSE (°C)	Bias (°C)	R^2
E-W, film side	18	1.25	1.36	+0.80	0.749
E-W, middle	18	1.63	1.83	+1.05	0.463
E-W, north-wall side	18	1.26	1.41	+1.06	0.275
N-S, film side	18	1.26	1.40	−0.20	0.719
N-S, middle	18	1.40	1.57	+1.10	0.371
N-S, north-wall side	18	1.36	1.49	+0.32	0.473
All six locations	108	1.36	1.52	+0.69	0.564

The sunny-day canopy-air comparison showed moderate agreement and a residual bias. No equivalent cloudy-day canopy-air evaluation was performed. The spatial fields are therefore interpreted as conditional model outputs rather than exact temperature predictions or independently validated fields.

3.10. Time-Resolved CFD Temperature Fields

The CFD fields show pre-sunrise cooling, morning warming, midday thermal contrast, and evening cooling. In each of Figures 18–23, one color scale applies to all six times and both ridge-layout blocks. Separate scales were used for each variable and weather case so that the smaller cloudy-day changes remain visible. Sunny fields developed stronger inter-row and surface gradients after sunrise; cloudy fields showed smaller variations (Figures 18–23). The simplified canopy-zone surface maps are model outputs, not measurements of leaf temperature or crop physiology.

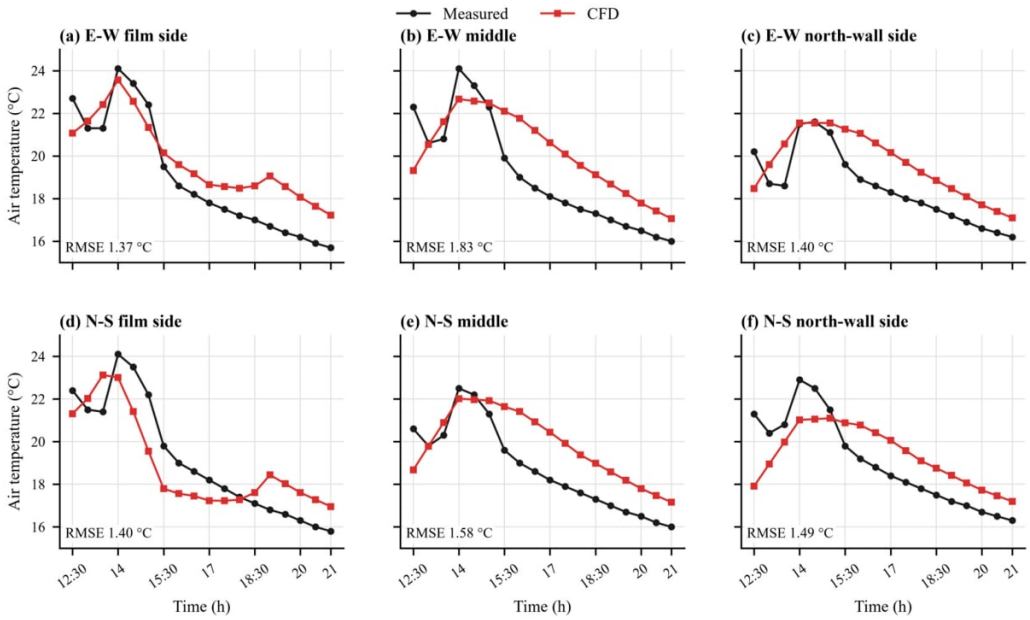


Figure 17. Measured and CFD-simulated canopy-air temperatures from 12:30 to 21:00 on 28 November 2025.

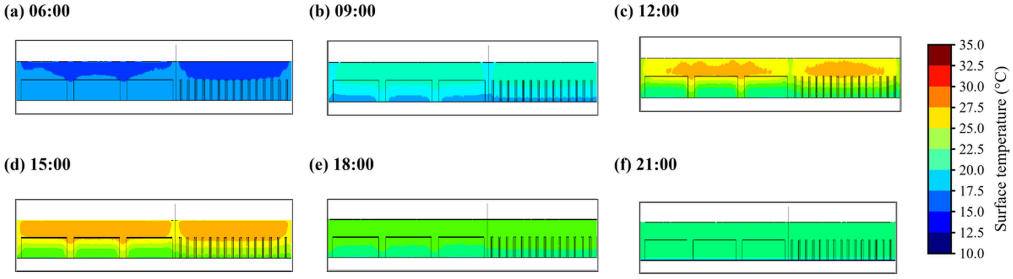


Figure 18. Sunny-case rear-wall temperature fields at 06:00, 09:00, 12:00, 15:00, 18:00, and 21:00. Panels (**a**–**f**) correspond to these times, respectively. The shared color bar indicates surface temperature (°C) and applies to all six panels. Black lines and boxes denote greenhouse structural boundaries and simplified ridge/canopy geometry; they do not represent additional temperature data.

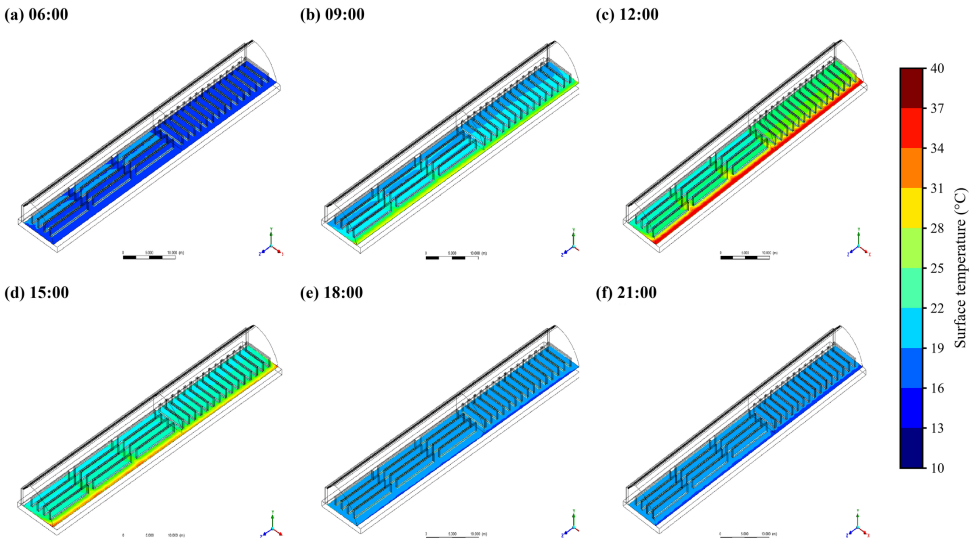


Figure 19. Sunny-case soil-surface temperature fields at 06:00, 09:00, 12:00, 15:00, 18:00, and 21:00. Panels (**a**–**f**) correspond to these times, respectively. The shared color bar indicates surface temperature (°C) and applies to all six panels. Black lines and boxes denote greenhouse structural boundaries and the simplified ridge/canopy geometry; they do not represent additional temperature data.

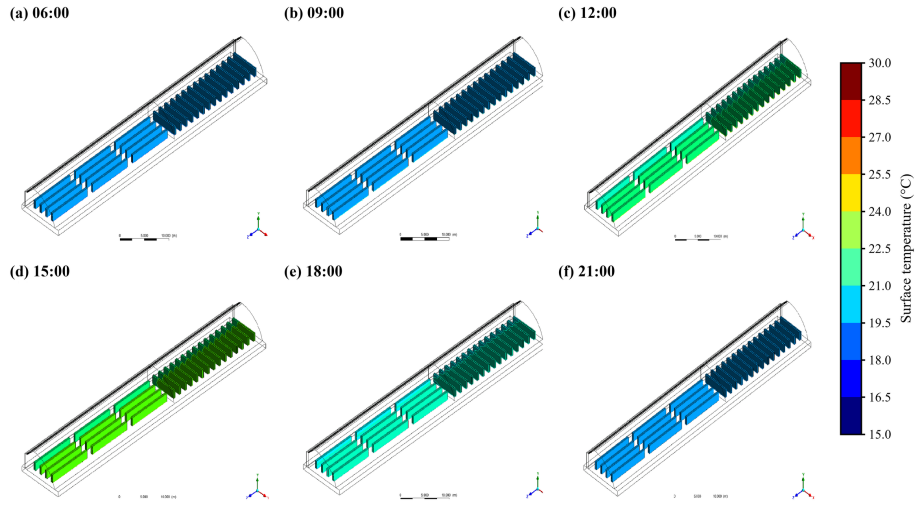


Figure 20. Sunny-case simplified canopy-zone surface temperature fields at 06:00, 09:00, 12:00, 15:00, 18:00, and 21:00. Panels (**a**–**f**) correspond to these times, respectively. The shared color bar indicates surface temperature (°C) and applies to all six panels. Black lines and boxes denote greenhouse structural boundaries and the simplified ridge/canopy geometry; they do not represent additional temperature data.

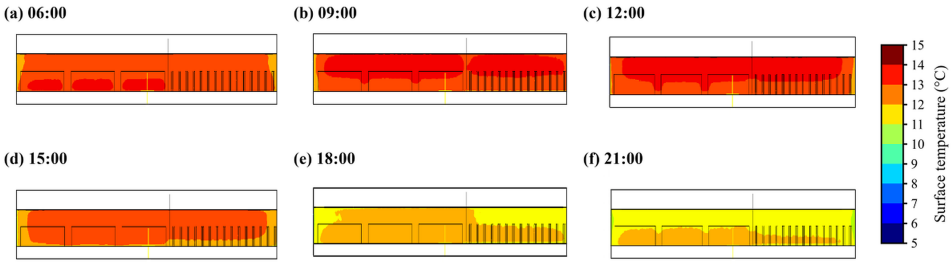


Figure 21. Cloudy-case rear-wall temperature fields at 06:00, 09:00, 12:00, 15:00, 18:00, and 21:00. Panels (**a**–**f**) correspond to these times, respectively. The shared color bar indicates surface temperature (°C) and applies to all six panels. Black lines and boxes denote greenhouse structural boundaries and simplified ridge/canopy geometry; they do not represent additional temperature data.

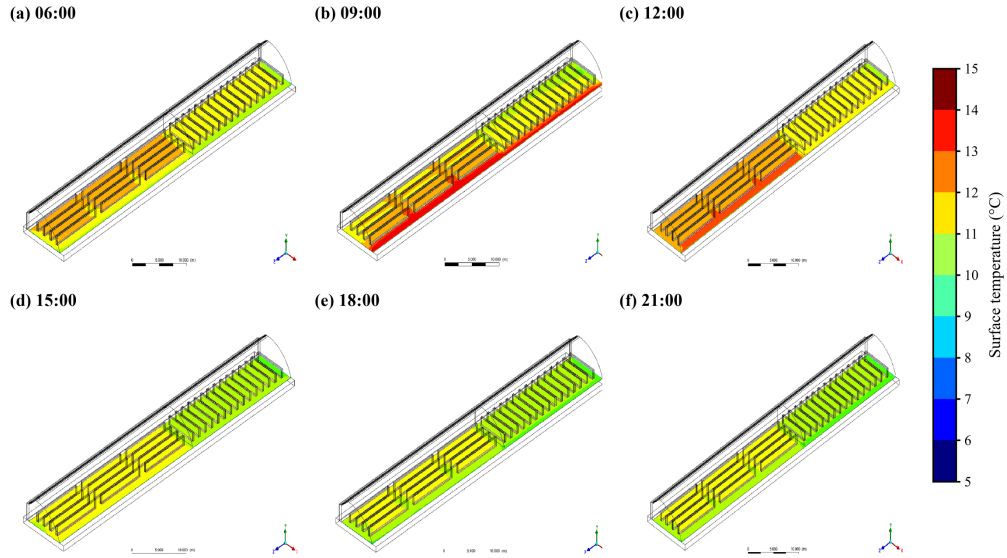


Figure 22. Cloudy-case soil-surface temperature fields at 06:00, 09:00, 12:00, 15:00, 18:00, and 21:00. Panels (**a**–**f**) correspond to these times, respectively. The shared color bar indicates surface temperature (°C) and applies to all six panels. Black lines and boxes denote greenhouse structural boundaries and the simplified ridge/canopy geometry; they do not represent additional temperature data.

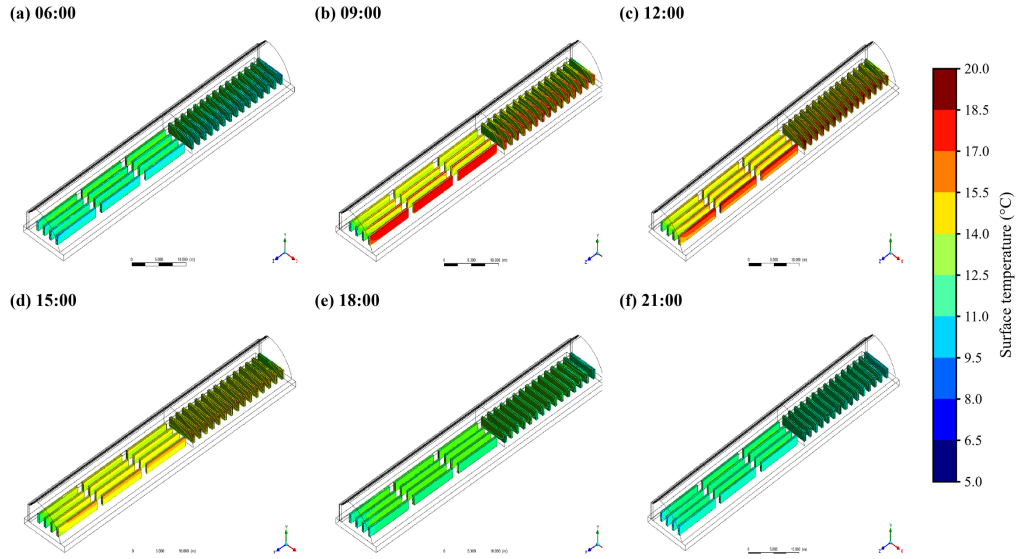


Figure 23. Cloudy-case simplified canopy-zone surface temperature fields at 06:00, 09:00, 12:00, 15:00, 18:00, and 21:00. Panels (**a**–**f**) correspond to these times, respectively. The shared color bar indicates surface temperature (°C) and applies to all six panels. Black lines and boxes denote greenhouse structural boundaries and the simplified ridge/canopy geometry; they do not represent additional temperature data.

3.11. CFD Interpretation of Layout-Related Patterns

The CFD results evaluated against measurements help interpret why the monitored blocks differed more at the soil surface than in mean canopy air. Modeled temperature differences were larger at the soil, film, and canopy surfaces than in the crop-zone air. These surface patterns followed the modeled distribution of solar exposure and row shading. Point-level departures can arise when the assumed optical properties of the plastic film, soil, masonry, and rear slope do not match their field conditions, including aging, dust, moisture, and surface texture. In addition, the experiment did not synchronously record ventilation rate, wind speed, or relative humidity, so the model could not reproduce the full air-exchange and convective heat-transfer state. Air density was fixed, so the simulated air movement also excluded buoyancy-driven flow.

4. Discussion

4.1. Layout Contrasts Were Stronger at the Soil Surface than in Canopy Air

Mean canopy-air temperature differed by only 0.12 °C between the two layouts over the observation period, whereas mean soil-surface temperature differed by 1.12 °C. The daytime soil-surface temperature difference increased to 2.48 °C on the cloudy day. This separation between air and soil-surface responses is consistent with the thermal inertia of the soil and other heat-storage components in CSGs [37]. Heat absorbed at the soil surface can remain spatially local even when mixing reduces the corresponding difference in canopy air. A greenhouse-wide air-temperature mean can therefore conceal a layout-related difference at the soil surface.

The soil-surface temperature contrast is potentially relevant to tomato production, but its biological meaning should not be overstated. Low root-zone temperature can restrict photosynthesis, root development, and mineral uptake in tomatoes. The temperatures controlled in the cited study were lower, and the exposure conditions differed from those in our greenhouse. We measured the soil surface rather than the full root-zone profile, and we did not measure root activity, nutrient uptake, growth, or yield. The present results

identify a thermal difference that warrants crop-level testing; they do not show that the warmer layout improved plant performance.

4.2. Thermal Contrasts Differed Between Representative Days

The calculated solar-elevation curves for 28 and 30 November were nearly identical, but the thermal responses were not. On the sunny day, the E-W block was associated with a warmer soil surface, while the N-S block showed stronger warming at the plastic film and north wall. On the cloudy response day, the film contrast largely disappeared, and the soil-surface difference became more pronounced. Solar position describes the direction of potential irradiance, not the radiation transmitted through a cloudy atmosphere or the greenhouse cover. Similar elevation curves therefore cannot explain the between-day contrast by themselves. Direct measurements of global and photosynthetically active radiation are needed to separate shading geometry from changing solar input.

Our small difference in mean canopy-air temperature should be interpreted alongside the study by Zhang et al., which investigated the effect of tomato crop-row orientation on the microclimate of a Chinese solar greenhouse using CFD simulation and numerical analysis. That work provides a numerical basis for treating row orientation as a greenhouse-microclimate design variable. The present study differs in its measurement-anchored evaluation and experimental scope. It combines field measurements with a CFD model evaluated against measurements, compares practical E-W and N-S ridge layouts during early winter, uses representative sunny-response and cloudy-response days, and evaluates soil-surface, rear-wall, rear-slope, plastic-film surface, and canopy-air temperatures. In the present study, CFD was used to test whether simulated fields reproduced measured temporal responses and then to support spatial interpretation. The two studies should therefore be distinguished by scope and evidence chain rather than treated as direct replications. Differences in ventilation, canopy development, ridge length, weather, and experimental design may also contribute to differences between their results.

4.3. Management Decisions Require a Thermal and Operational Balance

The experimental management followed common Chinese solar-greenhouse practice: a south-facing cover, a north heat-storage wall, night insulation, drip irrigation, and intermittent natural ventilation. Both blocks had the same tomato crop, 1.65 m ridge spacing, substrate-bag arrangement, and reported operating rules. The side-by-side E-W and N-S blocks with a 1.50 m passage and thin-film partition were a comparison arrangement, not a typical whole-greenhouse production layout. Under this shared management, the mean canopy-air difference was 0.12 °C and the mean soil-surface difference was 1.12 °C. Distributed surface measurements revealed a contrast that canopy-air monitoring alone would have missed. These observations do not establish a crop or mechanization advantage.

Ventilation exchanges sensible heat and changes local airflow, whereas irrigation can alter soil moisture, sensible heat storage, and evaporation. Brief vent events are likely to affect canopy air faster than the soil surface or north wall. The same operating rules were applied in both blocks, but differences in local airflow and surface exposure can still occur. The delivered water volume, vent flow, and event-level opening times were not continuously recorded, so their thermal effects cannot be separated quantitatively from the layout comparison.

4.4. CFD Supported Spatial Interpretation but Not Precise Prediction

CFD reproduced broad heating and cooling patterns at the evaluated locations, while point-level agreement varied. This use of CFD alongside distributed measurements is consistent with greenhouse modeling studies [38–44]. The largest sunny soil-surface RMSE

was 2.97 °C at the N-S position; the cloudy E-W soil-surface series had $R^2 = -0.33$ despite an RMSE of 0.94 °C. The latter reflects the narrow observed temperature range and illustrates why absolute errors should accompany R^2. Uncertain material properties, changing soil moisture, approximate ventilation, and simplified canopy shading can contribute to these differences. The model should not be used as an exact point predictor.

Fixed air density omitted buoyancy-driven airflow and associated temperature stratification. The canopy was treated as a continuous solid region without resolved leaves or transpiration. Retrospective wall Y+ means in the saved states were 0.010 at the crop interface, 0.020 at the plastic cover, 0.0097 at the inner north-wall surface, and 0.014 at the soil-side interface; the maximum sampled value was 1.61. These low values do not establish that the standard wall-function treatment adequately resolved near-wall airflow or convective transfer, particularly without a first-cell-height assessment. The first four time steps on each representative day also exceeded at least one retrospective flow or turbulence residual reference. These numerical limitations constrain mechanistic interpretation.

4.5. Limitations and Priorities for Further Work

This was a short comparison within one greenhouse. The E-W and N-S blocks were not independently replicated, and their ridges differed in length; their observed temperature differences cannot be assigned to orientation alone. The partition and aligned sensors reduced direct cross-block air exchange and positioning differences, but the film did not eliminate conductive or radiative heat transfer. Ten-minute records were serial observations, not independent replicates. Irradiance, wind, humidity, event-level ventilation, soil moisture, root-zone profiles, and crop responses were not monitored comprehensively. Material properties were not measured in situ, and canopy-air CFD comparison was limited to the sunny 12:30–21:00 interval. These limitations restrict generalization and the interpretation of simulated point temperatures. Future trials should use replicated blocks or greenhouses with matched ridge geometry and direct measurements of radiation, airflow, soil moisture, root-zone temperature, crop physiology, and yield [45–50].

Predictive modeling would require a broader, multivariable dataset collected across complete weather events, seasons, and preferably multiple greenhouses. Existing greenhouse forecasting work has relied on long winter sequences. Recent CSG studies used validation across several experiments [51]. Measurements from multiple greenhouse structures have also supported greenhouse forecasting [52]. The present 12-day record lacks irradiance, humidity, wind, soil-moisture, and control-state inputs and is therefore insufficient for a defensible predictive model. Future work should compare process-based and data-driven models with simple baselines, use event-level holdouts to prevent temporal leakage, report predictive uncertainty, and target a defined decision, such as cold-risk warning or heat-storage control.

5. Conclusions

This exploratory operational case study compared the thermal environments of E-W and N-S tomato ridge-layout blocks in one Chinese solar greenhouse during early winter. Using distributed field measurements and transient CFD, we examined where the observed thermal differences occurred and how they varied between representative sunny and cloudy conditions. The main findings are as follows.

1. During the 12-day observation period (22 November to 3 December 2025), mean canopy-air temperatures were 15.34 °C in the E-W block and 15.22 °C in the N-S block. Mean soil-surface temperatures were 14.43 and 13.31 °C, respectively. The observed thermal differences reflect the specific operational configurations of the E-W

and N-S blocks within the single greenhouse studied and should not be interpreted as a generalized or isolated causal effect of ridge orientation alone.

2. The largest observed between-block difference occurred at the soil surface rather than in canopy air. On the cloudy representative day (30 November), the daytime soil-surface temperature was 2.48 °C lower in the N-S block.
3. The two representative days had nearly identical calculated solar-elevation curves but different temperature responses. Because solar radiation was not measured, the contributions of cloud cover, atmospheric transmittance, and stored heat could not be separated.
4. The CFD model captured broad temporal patterns in soil-surface, rear-wall, and rear-slope temperatures on both representative days. Canopy-air temperature was evaluated only for the sunny day, from 12:30 to 21:00; no equivalent cloudy-day canopy-air evaluation was performed. Point-level agreement varied, and the model should not be treated as independently validated or as providing exact point predictions.
5. The soil surface in the E-W block was warmer during this early-winter observation. Because crop growth, root activity, physiological responses, and yield were not measured, the agronomic implications of this thermal difference remain undetermined.

Future studies should test these observed thermal associations in independently replicated greenhouse blocks across multiple greenhouses or seasons, with comparable ridge geometry and measurements of solar radiation, airflow, root-zone temperature, and crop responses. CFD studies should also document near-wall mesh resolution and residual convergence, and evaluate canopy-air temperatures under both sunny and cloudy conditions before drawing broader mechanistic or management conclusions.

Author Contributions: Conceptualization, Z.S., M.Y. (Mengmeng Yang) and W.L.; methodology, Z.S., W.S., M.Y. (Mengmeng Yang) and W.L.; software, Z.S., Q.W., X.D. and M.Y. (Mingze Yao); validation, Z.S., W.S. and M.Y. (Mengmeng Yang); formal analysis, Z.S. and W.S.; investigation, Z.S., W.S., Q.W., X.D., Y.C., Z.X., M.Y. (Mingze Yao) and F.Z.; resources, W.L.; data curation, Z.S. and W.S.; writing—original draft preparation, Z.S.; writing—review and editing, M.Y. (Mengmeng Yang), F.Z. and W.L.; visualization, Z.S.; supervision, M.Y. (Mengmeng Yang) and W.L.; project administration, W.L.; funding acquisition, W.L. All authors have read and agreed to the published version of the manuscript.

Funding: This research was supported by the Liaoning Provincial Joint Science and Technology Program (Natural Science Foundation-General Program, 2025-MSLH-616) and the Liaoning Revitalization Talents Program Agricultural Expert Project (grant No. XLYC2513021).

Institutional Review Board Statement: Not applicable.

Informed Consent Statement: Not applicable.

Data Availability Statement: The original contributions presented in this study are included in this article. Further inquiries can be directed to the corresponding authors.

Conflicts of Interest: The authors declare no conflicts of interest.

References

1. Bakker, J.C.; Bot, G.P.A.; Challa, H.; van de Braak, N.J. (Eds.) *Greenhouse Climate Control: An Integrated Approach*; Wageningen Academic Publishers: Wageningen, The Netherlands, 1995. [CrossRef]
2. Gao, L.H.; Qu, M.; Ren, H.Z.; Sui, X.L.; Chen, Q.Y.; Zhang, Z.X. Structure, function, application, and ecological benefit of a single-slope, energy-efficient solar greenhouse in China. *HortTechnology* **2010**, *20*, 626–631. [CrossRef]
3. Tong, G.; Christopher, D.M.; Li, B. Numerical modelling of temperature variations in a Chinese solar greenhouse. *Comput. Electron. Agric.* **2009**, *68*, 129–139. [CrossRef]
4. Tong, G.; Christopher, D.M.; Li, T.; Wang, T. Passive solar energy utilization: A review of cross-section building parameter selection for Chinese solar greenhouses. *Renew. Sustain. Energy Rev.* **2013**, *26*, 540–548. [CrossRef]

5. Weidner, T.; Yang, A.; Forster, F.; Hamm, M.W. Regional conditions shape the food-energy-land nexus of low-carbon indoor farming. *Nat. Food* **2022**, *3*, 206–216. [CrossRef] [PubMed]
6. Cao, K.; Xu, H.; Zhang, R.; Xu, D.; Yan, L.; Sun, Y.; Xia, L.; Zhao, J.; Zou, Z.; Bao, E. Renewable and sustainable strategies for improving the thermal environment of Chinese solar greenhouses. *Energy Build.* **2019**, *202*, 109414. [CrossRef]
7. Stanghellini, C. *Transpiration of Greenhouse Crops: An Aid to Climate Management*; Institute of Agricultural Engineering (IMAG): Wageningen, The Netherlands, 1987. [CrossRef]
8. Shamshiri, R.R.; Jones, J.W.; Thorp, K.R.; Ahmad, D.; Che Man, H.; Taheri, S. Review of optimum temperature, humidity, and vapour pressure deficit for microclimate evaluation and control in greenhouse cultivation of tomato: A review. *Int. Agrophys.* **2018**, *32*, 287–302. [CrossRef]
9. Katsoulas, N.; Stanghellini, C. Modelling crop transpiration in greenhouses: Different models for different applications. *Agronomy* **2019**, *9*, 392. [CrossRef]
10. Zhang, Y.; Yasutake, D.; Hidaka, K.; Kimura, K.; Okayasu, T.; Kitano, M.; Hirota, T. Eco-friendly strategy for CO_2 enrichment performance in commercial greenhouses based on the CO_2 spatial distribution and photosynthesis. *Sci. Rep.* **2023**, *13*, 17277. [CrossRef] [PubMed]
11. Miao, Y.N.; Ren, J.L.; Zhang, Y.; Chen, X.M.; Qi, M.F.; Li, T.L.; Zhang, G.X.; Liu, Y.F. Effect of low root-zone temperature on photosynthesis, root structure and mineral element absorption of tomato seedlings. *Sci. Hortic.* **2023**, *315*, 111956. [CrossRef]
12. van der Meer, M.; de Visser, P.H.B.; Heuvelink, E.; Marcelis, L.F.M. Row orientation affects the uniformity of light absorption, but hardly affects crop photosynthesis in hedgerow tomato crops. *In Silico Plants* **2021**, *3*, diab025. [CrossRef]
13. Abanay, A.; Masmoudi, L.; El Ansari, M.; Gonzalez-Jimenez, J.; Moreno, F.-A. LIDAR-based autonomous navigation method for an agricultural mobile robot in strawberry greenhouse: AgriEco Robot. *AIMS Electron. Electr. Eng.* **2022**, *6*, 317–328. [CrossRef]
14. Cheng, B.; He, X.; Li, X.; Zhang, N.; Song, W.; Wu, H. Research on positioning and navigation system of greenhouse mobile robot based on multi-sensor fusion. *Sensors* **2024**, *24*, 4998. [CrossRef] [PubMed]
15. Zhang, C.; Liu, R.; Yang, J.; Rodríguez Díaz, F.; Li, M. Assessing the impact of tomato crop row orientation on the microclimate in Chinese solar greenhouses: CFD simulation and numerical analysis. *Biosyst. Eng.* **2025**, *258*, 104247. [CrossRef]
16. Zhang, X.; Wang, H.; Zou, Z.; Wang, S. CFD and weighted entropy based simulation and optimisation of Chinese Solar Greenhouse temperature distribution. *Biosyst. Eng.* **2016**, *142*, 12–26. [CrossRef]
17. Tong, G.; Christopher, D.M.; Zhang, G. New insights on span selection for Chinese solar greenhouses using CFD analyses. *Comput. Electron. Agric.* **2018**, *149*, 3–15. [CrossRef]
18. Boulard, T.; Wang, S. Greenhouse crop transpiration simulation from external climate conditions. *Agric. For. Meteorol.* **2000**, *100*, 25–34. [CrossRef]
19. Boulard, T.; Wang, S. Experimental and numerical studies on the heterogeneity of crop transpiration in a plastic tunnel. *Comput. Electron. Agric.* **2002**, *34*, 173–190. [CrossRef]
20. Zhang, Y.; Henke, M.; Li, Y.; Yue, X.; Xu, D.; Liu, X.; Li, T. High resolution 3D simulation of light climate and thermal performance of a solar greenhouse model under tomato canopy structure. *Renew. Energy* **2020**, *160*, 730–745. [CrossRef]
21. Reda, I.; Andreas, A. Solar position algorithm for solar radiation applications. *Sol. Energy* **2004**, *76*, 577–589. [CrossRef]
22. Spencer, J.W. Fourier series representation of the position of the sun. *Search* **1971**, *2*, 172.
23. Iqbal, M. *An Introduction to Solar Radiation*; Academic Press: Toronto, ON, Canada, 1983. [CrossRef]
24. Duffie, J.A.; Beckman, W.A. *Solar Engineering of Thermal Processes*, 4th ed.; John Wiley & Sons: Hoboken, NJ, USA, 2013. [CrossRef]
25. Norton, T.; Sun, D.W.; Grant, J.; Fallon, R.; Dodd, V. Applications of computational fluid dynamics (CFD) in the modelling and design of ventilation systems in the agricultural industry: A review. *Bioresour. Technol.* **2007**, *98*, 2386–2414. [CrossRef] [PubMed]
26. Reichrath, S.; Davies, T.W. Using CFD to model the internal climate of greenhouses: Past, present and future. *Agronomie* **2002**, *22*, 3–19. [CrossRef]
27. Bournet, P.E.; Boulard, T. Effect of ventilator configuration on the distributed climate of greenhouses: A review of experimental and CFD studies. *Comput. Electron. Agric.* **2010**, *74*, 195–217. [CrossRef]
28. ANSYS, Inc. *ANSYS Fluent Theory Guide, Release 2021 R2*; ANSYS, Inc.: Canonsburg, PA, USA, 2021.
29. Mistriotis, A.; Arcidiacono, C.; Picuno, P.; Bot, G.P.A.; Scarascia-Mugnozza, G. Computational analysis of ventilation in greenhouses at zero- and low-wind-speeds. *Agric. For. Meteorol.* **1997**, *88*, 121–135. [CrossRef]
30. Kittas, C.; Boulard, T.; Papadakis, G. Natural ventilation of a greenhouse with ridge and side openings: Sensitivity to temperature and wind effects. *Trans. ASAE* **1997**, *40*, 415–425. [CrossRef]
31. Kacira, M.; Short, T.H.; Stowell, R.R. A CFD evaluation of naturally ventilated, multi-span, sawtooth greenhouses. *Trans. ASAE* **1998**, *41*, 833–836. [CrossRef]
32. Majdoubi, H.; Boulard, T.; Fatnassi, H.; Bouirden, L. Airflow and microclimate patterns in a one-hectare Canary type greenhouse: An experimental and CFD assisted study. *Agric. For. Meteorol.* **2009**, *149*, 1050–1062. [CrossRef]
33. Teitel, M.; Ziskind, G.; Liran, O.; Dubovsky, V.; Letan, R. Effect of wind direction on greenhouse ventilation rate, airflow patterns and temperature distributions. *Biosyst. Eng.* **2008**, *101*, 351–369. [CrossRef]

34. Piscia, D.; Montero, J.I.; Baeza, E.; Bailey, B.J. A CFD greenhouse night-time condensation model. *Biosyst. Eng.* **2012**, *111*, 141–154. [CrossRef]
35. Baeza, E.J.; Perez-Parra, J.J.; Lopez, J.C.; Gazquez, J.C.; Kacira, M.; Montero, J.I. Validation of CFD simulations for three-dimensional temperature distributions of a naturally ventilated multispan greenhouse obtained by wind tunnel measurements. *Acta Hortic.* **2011**, *893*, 571–579. [CrossRef]
36. Romero-Gomez, P.; Lopez-Cruz, I.L.; Choi, C.Y. Analysis of greenhouse natural ventilation under the environmental conditions of central Mexico. *Trans. ASABE* **2008**, *51*, 1753–1761. [CrossRef]
37. Zhang, Y.; Xu, L.; Zhu, X.; He, B.; Chen, Y. Thermal environment model construction of Chinese solar greenhouse based on temperature-wave interaction theory. *Energy Build.* **2023**, *279*, 112648. [CrossRef]
38. Bartzanas, T.; Boulard, T.; Kittas, C. Effect of vent arrangement on windward ventilation of a tunnel greenhouse. *Biosyst. Eng.* **2004**, *88*, 479–490. [CrossRef]
39. Fatnassi, H.; Boulard, T.; Bouirden, L. Simulation of climatic conditions in full-scale greenhouse fitted with insect-proof screens. *Agric. For. Meteorol.* **2003**, *118*, 97–111. [CrossRef]
40. Boulard, T.; Kittas, C.; Roy, J.C.; Wang, S. Convective and ventilation transfers in greenhouses, Part 2: Determination of the distributed greenhouse climate. *Biosyst. Eng.* **2002**, *83*, 129–147. [CrossRef]
41. Fatnassi, H.; Boulard, T.; Poncet, C.; Chave, M. Optimisation of greenhouse insect screening with computational fluid dynamics. *Biosyst. Eng.* **2006**, *93*, 301–312. [CrossRef]
42. Lee, I.B.; Bitog, J.P.P.; Hong, S.W.; Seo, I.H.; Kwon, K.S.; Bartzanas, T.; Kacira, M. The past, present and future of CFD for agro-environmental applications. *Comput. Electron. Agric.* **2013**, *93*, 168–183. [CrossRef]
43. Bournet, P.E.; Rojano, F. Advances of Computational Fluid Dynamics (CFD) applications in agricultural building modelling: Research, applications and challenges. *Comput. Electron. Agric.* **2022**, *201*, 107277. [CrossRef]
44. Si, C.; Qi, F.; Ding, X.; He, F.; Gao, Z.; Feng, Q.; Zheng, L. CFD analysis of solar greenhouse thermal and humidity environment considering soil-crop-back wall interactions. *Energies* **2023**, *16*, 2305. [CrossRef]
45. He, M.; Sun, D.; Wen, P.; Sun, Y.; Li, T.; Li, Y.; Liu, X. Environmental control for Chinese solar greenhouses: A review. *Renew. Sustain. Energy Rev.* **2025**, *218*, 115796. [CrossRef]
46. Ding, D. Design strategies of passive solar greenhouses: A bibliometric and systematic review. *Ain Shams Eng. J.* **2024**, *15*, 102680. [CrossRef]
47. Zhao, L.; Shui, Z.; Liu, X.; Yang, T.; Duan, G. Computer-aiding evaluation of north wall effects of a solar greenhouse: Multiphysics modelling of the indoor environment. *Case Stud. Therm. Eng.* **2024**, *64*, 105361. [CrossRef]
48. Zhang, Z.; Li, Y.; Wang, L.; Cheng, W.; Liu, Z. A study of the soil-wall-indoor air thermal environment in a solar greenhouse. *Sensors* **2025**, *25*, 4041. [CrossRef] [PubMed]
49. Ma, Q.; Zhu, D.; Sun, W.; Zong, C.; Li, H.; Yu, J.; Song, W.; Wei, X. Temperature predictive modeling using machine learning for thermal parameter design of Chinese solar greenhouses. *Appl. Therm. Eng.* **2026**, *300*, 131538. [CrossRef]
50. Shi, C.; He, M.; Liu, H.; Liu, F.; Lin, T.; Li, T.; Li, Y.; Liu, X. Natural ventilation in mechanized solar greenhouses: A CFD modeling study on cultivation pattern modification. *Appl. Therm. Eng.* **2026**, *302*, 131795. [CrossRef]
51. Zhou, B.; Reyes Lastiri, D.; Wang, N.; Yang, Q.; van Henten, E.J. An open-source indoor climate and yield prediction model for Chinese solar greenhouses. *Biosyst. Eng.* **2025**, *250*, 183–212. [CrossRef]
52. Yu, J.; Zhao, J.; Sun, C.; Zhang, R.; Zheng, W.; Xu, L.; Wei, X. A dual deep learning approach for winter temperature prediction in solar greenhouses in Northern China. *Comput. Electron. Agric.* **2025**, *229*, 109807. [CrossRef]

Disclaimer/Publisher's Note: The statements, opinions and data contained in all publications are solely those of the individual author(s) and contributor(s) and not of MDPI and/or the editor(s). MDPI and/or the editor(s) disclaim responsibility for any injury to people or property resulting from any ideas, methods, instructions or products referred to in the content.